A radio transient with unusually slow periodic emission

https://doi.org/10.1038/s41586-021-04272-x

Received: 30 July 2021

Accepted: 19 November 2021

N. Hurley-Walker[1]✉, X. Zhang[2,3], A. Bahramian[1], S. J. McSweeney[1], T. N. O'Doherty[1], P. J. Hancock[1], J. S. Morgan[1], G. E. Anderson[1], G. H. Heald[2] & T. J. Galvin[1]

The high-frequency radio sky is bursting with synchrotron transients from massive stellar explosions and accretion events, but the low-frequency radio sky has, so far, been quiet beyond the Galactic pulsar population and the long-term scintillation of active galactic nuclei. The low-frequency band, however, is sensitive to exotic coherent and polarized radio-emission processes, such as electron-cyclotron maser emission from flaring M dwarfs[1], stellar magnetospheric plasma interactions with exoplanets[2] and a population of steep-spectrum pulsars[3], making Galactic-plane searches a prospect for blind-transient discovery. Here we report an analysis of archival low-frequency radio data that reveals a periodic, low-frequency radio transient. We find that the source pulses every 18.18 min, an unusual periodicity that has, to our knowledge, not been observed previously. The emission is highly linearly polarized, bright, persists for 30–60 s on each occurrence and is visible across a broad frequency range. At times, the pulses comprise short-duration (<0.5 s) bursts; at others, a smoother profile is observed. These profiles evolve on timescales of hours. By measuring the dispersion of the radio pulses with respect to frequency, we have localized the source to within our own Galaxy and suggest that it could be an ultra-long-period magnetar.

We searched 24 h of Galactic-plane observations taken by the Murchison Widefield Array (MWA; see Methods) using a rapid shallow-search method to probe a previously undescribed transient-timescale parameter space (P.J.H., manuscript in preparation). From this search, we discovered the transient source, Galactic and Extragalactic All-sky MWA – Extended (GLEAM-X) J162759.5-523504.3, initially with two high-signal-to-noise detections. A further, exhaustive search yielded 71 pulses spanning January to March 2018 (Fig. 1), with maximum flux densities ranging from 5 to 40 Jy (Fig. 2). The pulse widths range between 30 and 60 s and evolve on hourly timescales, sometimes comprising many 'spiky' bursts unresolved at our time resolution of 0.5 s, other times displaying sub-pulses with widths of 10–30 s. Aligning the pulses, we established a period of 1,091.1690 ± 0.0005 s (see Methods). It was necessary to perform a barycentric correction, indicating an extrasolar origin.

Using data with a range of 72–231 MHz, we established a dispersion measure of 57 ± 1 pc cm^{-3} (see Methods and Extended Data Fig. 1), which, when combined with Galactic electron-density models[4], produces a distance estimate of 1.3 ± 0.5 kpc. We also measured a radio spectral index of $\alpha = -1.16 \pm 0.04$, where the flux density $S_\nu \propto \nu^\alpha$, indicating that the emission is non-thermal. Brightness variations on timescales of less than 0.5 s suggest a compact object and the brightness temperature of a thermal object 0.5 light seconds in size producing 20 Jy of flux density at 1.3 kpc is about 10^{16} K, implying a coherent emission mechanism.

The pulses exhibit a constant, high-fractional linear polarization (88 ± 1%) and there is no change in polarization angle as a function of either the pulse phase or the observation time (Fig. 3). The Faraday rotation measure (RM) remains constant over the observations at -61 ± 1 rad m^{-2}, which is consistent with the Galactic RM towards this region[5] (-72.3 ± 154.9 rad m^{-2}).

The fluence of the pulses is variable but broadly follows a distribution with two 'on' intervals approximately 30 days wide (3 January–2 February and 28 February–28 March 2018; see Fig. 2), with fast rise times, slow decay times and a 26-day null interval between them. The detections are all serendipitous in archival data, leading to heterogeneous coverage. During the on intervals, at every time when we predict we would detect a pulse, we do so (that is, there is no obvious nulling). The flux density in 30-s images at the source location is <10 mJy during the sampled 'off' intervals (upper limits in Fig. 2). Although the fluence variation does resemble gravitational lensing[6] or extreme scattering events[7], the magnification required would be on the order 1,000× and would be difficult to create with any physically plausible gravitational or plasma lens.

The high linear polarization indicates the presence of strongly ordered magnetic fields; this and the luminosity of the pulses are not explicable by known phenomena such as radio emission from flare stars[8], exoplanets[9] and white-dwarf/M-dwarf binaries[10], all of which would be orders of magnitude fainter at this distance, and would typically be circularly polarized. The extreme regularity of the emission (fractional uncertainty $\frac{\sigma_P}{P} < 5 \times 10^{-7}$, where σ_P is the error on P, its measured period; see Methods) implies either a rotational or an orbital origin. Owing to the 0.5-light-second upper limit on the object's size, a rotational origin may be more likely.

---

[1] International Centre for Radio Astronomy Research (ICRAR), Curtin University, Bentley, Western Australia, Australia. [2] CSIRO, Space and Astronomy, Bentley, Western Australia, Australia. [3] Shanghai Astronomical Observatory, Chinese Academy of Sciences, Shanghai, China. ✉e-mail: nhw@icrar.org

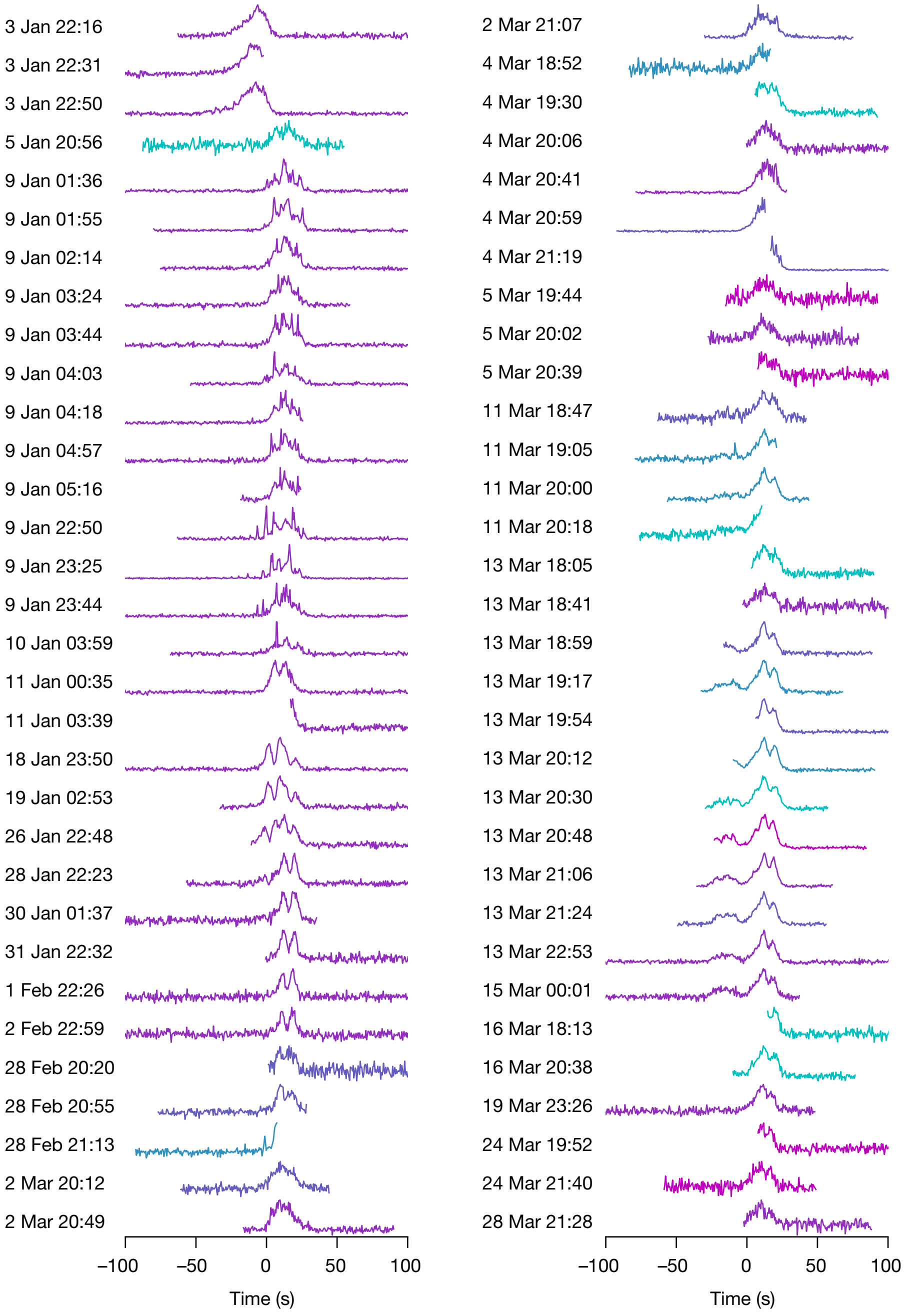

Fig. 1 | Sixty-four of the 71 detected pulses of GLEAM-X J162759.5-523504.3 aligned to its measured period P and period derivative $\dot{P}$. Omitted pulses were truncated or had a signal-to-noise ratio that was too low to be displayed here; flux densities are normalized to the peak of each pulse for readability; barycentric and dispersive corrections have been applied. The observation start times in coordinated universal time are listed on the left of each detection. The colour range spans 88 MHz (cyan) to 215 MHz (magenta) and the detections span 84 days in January to March 2018. The pulses observed on 3 January 2018 are not misaligned and fit within the widest pulse windows found on 13 March 2018 (see Methods).

Figure 4 shows GLEAM-X J162759.5-523504.3 in context with other sources of transient emission. The source that bears the most similarity to GLEAM-X J162759.5-523504.3 is GCRT 1745, a transient radio source detected towards the Galactic Centre with observations at 330 MHz, which exhibited five 10-min-duration bursts with periodicity 77 min (ref. [11]). These bursts exhibited slow profile evolution and low circular polarization (no linear polarization measurements were available). Owing to the crowded field in this direction, and lack of distance constraints, Hyman et al.[11] were unable to determine a progenitor but speculated that it may be a long-period magnetar, an interpretation that can be applied to GLEAM-X J162759.5-523504.3.

Magnetic neutron stars rotating at period P lose energy via magnetic-dipole radiation, causing them to spin down (that is, they have a positive period derivative $\dot{P}$); this spin-down luminosity ($\dot{E}$) can be expressed as $\frac{4\pi^2 I\dot{P}}{P^3}$, where I is the neutron star moment of inertia, typically assumed to be 10^{45} g cm^{-2}. Via a grid search for P and $\dot{P}$ (see Methods), we find that $\dot{P} > 0$ is preferred, the best-fit value is $\dot{P} = 6 \times 10^{-10}$ s s^{-1} and the analysis favours $\dot{P} < 1.2 \times 10^{-9}$ s s^{-1} (see Extended Data Fig. 7 for context with known neutron stars). Using this value as an upper limit, we find a maximum spin-down luminosity of $\dot{E} < 1.2 \times 10^{28}$ erg s^{-1}. The flux density of radio pulsars can be converted to a luminosity (see Methods), which—for the brightest pulses from GLEAM-X J162759.5-523504.3—is 4×10^{31} erg s^{-1}. Pulsar radio luminosities are typically a small fraction

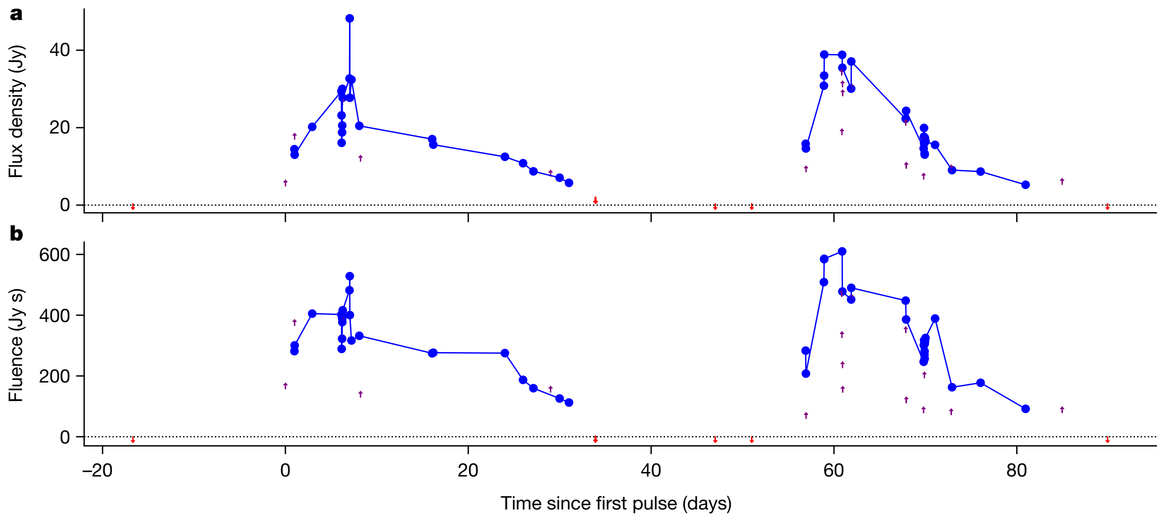

Fig. 2 | Maximum brightness of each pulse and total pulse fluence as a function of time across the two observed intervals of activity. a, Maximum brightness of each pulse. **b**, Total pulse fluence. Not all pulses are fully captured by every observation; in these cases, lower limits are plotted with purple, upward-pointing arrows. Observations in which the source was within the field of view and predicted to be detectable, but not found, are shown with red, downward-pointing arrows equal to the root-mean-square noise in a 30-s image corresponding to the time at which a pulse was expected. All measurements have been scaled to a common frequency of 154 MHz via the spectral index $\alpha = -1.16$. Error bars are omitted for clarity and are dominated by the approximately 5% uncertainty in the primary beam model of the telescope.

of their spin-down luminosities[12], whereas this source exhibits the reverse, indicating that the emission is not generated purely by spin down. Additionally, the smooth variations in pulse profile and the transient window of radio emission are more consistent with the interpretation of GLEAM-X J162759.5-523504.3 as a radio magnetar than a pulsar[13].

Magnetars are commonly detected and characterized via X-ray observations; four of the five known magnetars that have produced detectable pulsed radio emissions have done so only after X-ray outbursts. However, not all X-ray-emitting magnetars produce detectable radio emissions. Previous studies have shown that magnetars only produce radio emissions if their quiescent X-ray luminosity in the 0.5–10-keV band is lower than their spin-down luminosity[14]. We would, therefore, predict that the X-ray luminosity L_X of GLEAM-X J162759.5-523504.3 is $<6 \times 10^{27}$ erg s^{-1}. We obtained X-ray observations with the Swift X-Ray Telescope (XRT) and determined that $L_X < 10^{32}$ erg s^{-1} (see Methods), which—although not a strong limit compared with our expectation under this interpretation—is a lower quiescent X-ray luminosity than all but two of the faintest known magnetars[15], SGR 0418+5729 and Swift J1822.3−1606. Alternatively, a white dwarf would have a moment of inertia and therefore a spin-down luminosity 10^5 times larger, allowing the possibility of spin-powered radio pulsations; deeper ultraviolet and infrared observations than currently available would test this hypothesis.

Regardless of interpretation, the existence of an unexpected slowly pulsating yet intermittent radio transient opens up a new field of exploration of radio surveys, particularly at low frequencies. Whereas many sensitive low-frequency ($\lesssim$340 MHz) continuum surveys have searched for transients on cadences of minutes within extragalactic fields for up to an hour at a time, no such systematic survey for unknown minute-period transients has been conducted within the Galactic plane on similar timescales[16–20]. As known pulsars and magnetars have periods of $\lesssim$10 s, surveys are typically designed with relatively short dwell times

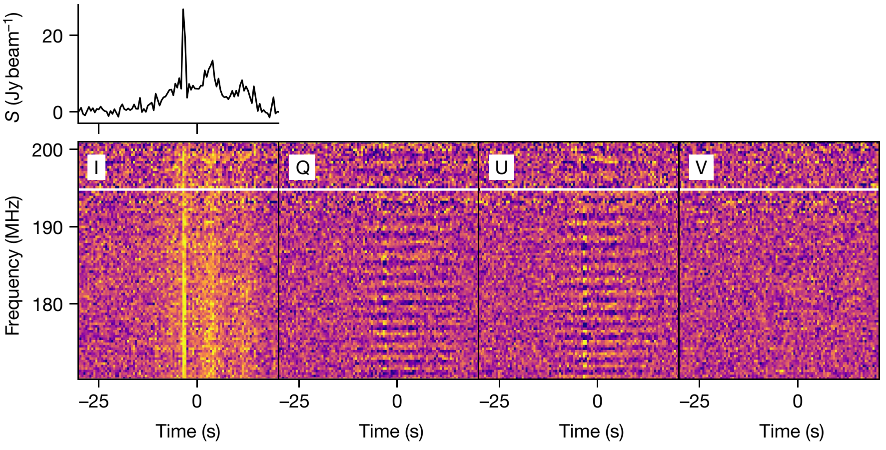

Fig. 3 | Dynamic spectrum of the observation recorded at 03:59 on 10 January 2018. From left to right, the panels show the Stokes I, Q, U and V flux density as a function of frequency and time, with a dispersion correction of 57 pc cm^{-3} applied. Linear Stokes Q and U show Faraday rotation of −61 ± 1 rad m^{-2}, whereas circular V shows no obvious signal. The top-left panel of the image shows the profile of the Stokes I data averaged over the frequency axis; the unresolved burst of emission shows the limitation of our 0.5-s time resolution. The root mean square of the noise in each spectrum is 8.5 Jy beam^{-1}, and in the summed profile is and 0.9 Jy beam^{-1}.

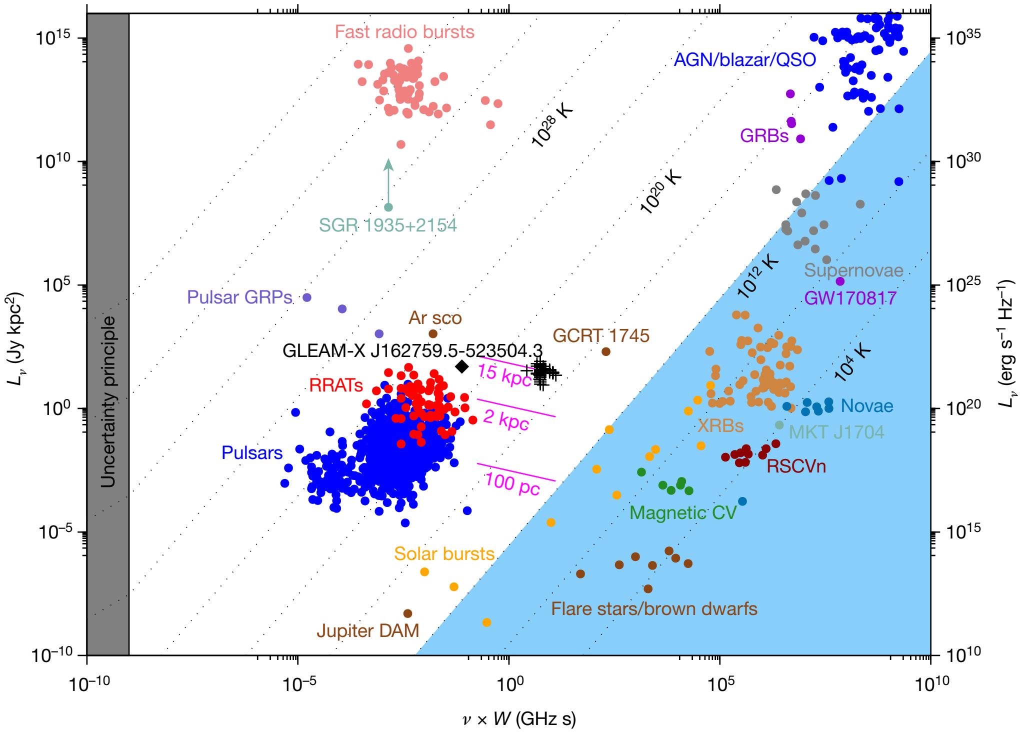

Fig. 4 | Transient parameter space populated with common known radio transients. Radio pseudo-luminosity is shown on the y axes and the product of observing frequency ν and transient/variability timescale W is plotted on the x axis. The shaded blue region shows objects with brightness temperatures that do not imply coherent emission mechanisms. The '+' symbols show the $W = 30$–60-s pulses of GLEAM-X J162759.5-523504.3; the diamond indicates a representative unresolved pulse of $W = 0.5$ s and $S = 30$ Jy. Diagonal magenta lines show the sensitivity of the MWA to long-pulse transients at Galactic distances, for $W = 2$–60 s across the range 72–231 MHz, with dispersion-measure smearing effects included. Figure adapted from Pietka et al.[24].

of around 100–5,000 s (ref. [21]) and use high-pass filters to mitigate red telescope noise[22], rendering them insensitive to long-period sources. Current MWA survey strategies[19,23] may, therefore, be sensitive to a large population of these sources and further detections may explain some of the other puzzling, unidentified low-frequency Galactic transients[11].

We can estimate the population of similar long-period transients detectable with future searches starting from the following assumptions: like other first detections of a new class of object, GLEAM-X J162759.5-523504.3 is the most luminous example of its kind; the luminosity and spatial distribution of the population are similar to that of pulsars; other sources would have similar long-term duty cycles of about 2% (see Methods). Now that we are aware of this class of objects, it is worth the computational expense of performing model-subtracting time-step imaging (see Methods) and searching all voxels for notable residuals, a technique that is ten times more sensitive than the fast search that detected GLEAM-X J162759.5-523504.3 (see diagonal magenta lines in Fig. 4). With these population assumptions, and using this technique, we predict approximately ten further detections of similar objects in the same volume of data that yielded GLEAM-X J162759.5-523504.3 (24 h). Larger duty cycles or a flatter luminosity distribution would increase this number. The MWA archive contains thousands of hours of observing time sensitive to $|b| < 10°$, which may yield hundreds of further similar objects; this will also be true of other radio archives with data covering the Galactic plane. Further detections and rapid, high-time-resolution follow-up of candidates will more conclusively determine the nature of these sources, thus, providing further insight into the evolutionary extremes surrounding the life and death of massive stars.

Online content

Any methods, additional references, Nature Research reporting summaries, source data, extended data, supplementary information, acknowledgements, peer review information; details of author contributions and competing interests; and statements of data and code availability are available at https://doi.org/10.1038/s41586-021-04272-x.

1. Lynch, C. R., Lenc, E., Kaplan, D. L., Murphy, T. & Anderson, G. E. 154 MHz detection of faint, polarized flares from UV Ceti. *Astrophys. J. Lett.* **836**, L30 (2017).
2. Vedantham, H. K. et al. Coherent radio emission from a quiescent red dwarf indicative of star–planet interaction. *Nat. Astron.* **4**, 577–583 (2020).
3. Swainston, N. A. et al. Discovery of a steep-spectrum low-luminosity pulsar with the Murchison Widefield Array. *Astrophys. J. Lett.* **911**, L26 (2021).
4. Yao, J. M., Manchester, R. N. & Wang, N. A new electron-density model for estimation of pulsar and FRB distances. *Astrophys. J.* **835**, 29 (2017).
5. Hutschenreuter, S. & Enßlin, T. A. The Galactic Faraday depth sky revisited. *Astron. Astrophys.* **633**, A150 (2020).
6. Vedantham, H. K. et al. Symmetric achromatic variability in active galaxies: a powerful new gravitational lensing probe? *Astrophys. J.* **845**, 89 (2017).
7. Bannister, K. W. et al. Real-time detection of an extreme scattering event: constraints on Galactic plasma lenses. *Science* **351**, 354–356 (2016).
8. Benz, A. O. & Güdel, M. Physical processes in magnetically driven flares on the Sun, stars, and young stellar objects. *Annu. Rev. Astron. Astrophys.* **48**, 241–287 (2010).
9. Zarka, P., Treumann, R. A., Ryabov, B. P. & Ryabov, V. B. Magnetically-driven planetary radio emissions and application to extrasolar planets. *Astrophys. Space Sci.* **277**, 293–300 (2001).
10. Marsh, T. R. et al. A radio-pulsing white dwarf binary star. *Nature* **537**, 374–377 (2016).
11. Hyman, S. D. et al. A powerful bursting radio source towards the Galactic Centre. *Nature* **434**, 50–52 (2005).
12. Szary, A., Zhang, B., Melikidze, G. I., Gil, J. & Xu, R.-X. Radio efficiency of pulsars. *Astrophys. J.* **784**, 59 (2014).
13. Levin, L. et al. Radio emission evolution, polarimetry and multifrequency single pulse analysis of the radio magnetar PSR J1622–4950. *Mon. Not. R. Astron. Soc.* **422**, 2489–2500 (2012).
14. Rea, N., Pons, J. A., Torres, D. F. & Turolla, R. The fundamental plane for radio magnetars. *Astrophys. J. Lett.* **748**, L12 (2012).
15. Olausen, S. A. & Kaspi, V. M. The McGill magnetar catalog. *Astrophys. J. Suppl.* **212**, 6 (2014).
16. Carbone, D. et al. New methods to constrain the radio transient rate: results from a survey of four fields with LOFAR. *Mon. Not. R. Astron. Soc.* **459**, 3161–3174 (2016).
17. Polisensky, E. et al. Exploring the transient radio sky with VLITE: early results. *Astrophys. J.* **832**, 60 (2016).
18. Stewart, A. J. et al. LOFAR MSSS: detection of a low-frequency radio transient in 400 h of monitoring of the North Celestial Pole. *Mon. Not. R. Astron. Soc.* **456**, 2321–2342 (2016).

19. Bell, M. E. et al. The Murchison Widefield Array Transients Survey (MWATS). A search for low-frequency variability in a bright Southern Hemisphere sample. *Mon. Not. R. Astron. Soc.* **482**, 2484–2501 (2019).
20. Hajela, A., Mooley, K. P., Intema, H. T. & Frail, D. A. A GMRT 150 MHz search for variables and transients in Stripe 82. *Mon. Not. R. Astron. Soc.* **490**, 4898–4906 (2019).
21. Keith, M. J. et al. The High Time Resolution Universe Pulsar Survey – I. System configuration and initial discoveries. *Mon. Not. R. Astron. Soc.* **409**, 619–627 (2010).
22. Cameron, A. D., Barr, E. D., Champion, D. J., Kramer, M. & Zhu, W. W. An investigation of pulsar searching techniques with the fast folding algorithm. *Mon. Not. R. Astron. Soc.* **468**, 1994–2010 (2017).
23. Hurley-Walker, N. et al. Galactic and Extragalactic All-sky Murchison Widefield Array (GLEAM) survey – I. A low-frequency extragalactic catalogue. *Mon. Not. R. Astron. Soc.* **464**, 1146–1167 (2017).
24. Pietka, M., Fender, R. P. & Keane, E. F. The variability time-scales and brightness temperatures of radio flares from stars to supermassive black holes. *Mon. Not. R. Astron. Soc.* **446**, 3687–3696 (2015).

Methods

Observations

The MWA is a low-frequency radio telescope operating in the Murchison region of Western Australia[25,26]. At the time of the observation during which GLEAM-X J162759.5-523504.3 was discovered, it was engaged in observing the GLEAM-X survey, a follow-up to the GLEAM survey[27]. The data were taken in a drift-scan mode, iterating through a 72–231-MHz bandwidth by dwelling for 2 min in each of five 30.72-MHz bands, yielding a resolution of 5′–45″ and snapshot noise levels of 150–25 mJy beam^{-1}. Over this bandwidth, the field of view of the instrument is 60°–25° across, yielding multiple measurements of sources drifting through the primary beam. The data are sampled at 0.5-s time resolution and 10-kHz frequency resolution. We downloaded measurement sets from the MWA All-Sky Virtual Observatory (https://asvo.mwatelescope.org/) and, at this stage, averaged the data to 40 kHz to reduce data size and decrease processing times.

The initial detection of the transient was made by performing a differencing of the visibilities between observations taken at an identical local sidereal time several months apart (P.J.H., manuscript in preparation). Two detections were made and, based on the non-detections in adjacent observations, an initial period was determined. Including a barycentric correction, and searching the archive thoroughly between July 2017 and July 2018, the interval of activity was established to be January 2018 to March 2018, with a total of 71 detections (see Methods for further details on searching the MWA archive).

Calibration and imaging

For all data, calibration was performed using the Mitchcal algorithm[28] to derive antenna gains by comparing the raw data to model visibilities formed by a sky model based on catalogues derived from GLEAM[23,29]. These were applied to the observations and deep imaging was subsequently performed using WSClean[30] version 2.9.0, creating a visibility model that includes the spectrally variant primary beam. A 10′ × 10′ region around GLEAM-X J162759.5-523504.3 was masked during this process, so that the source was not included in the model.

After the deep model was created and subtracted from the visibilities, the data were re-imaged such that the transient was the only source in the field. The data were imaged at 320-kHz frequency resolution and 0.5-s time resolution in full Stokes (I, Q, U, V), which were formed from the instrumental data by application of the MWA beam model[31]. We also used observations from a polarization calibrator (PKS J0636−2036) to correct radio emission leaking from Stokes U into Stokes V (X–Y phase calibration[32]).

Dispersion measure

Because strong pulse-profile evolution is observed, we used the five observations that spanned 72–231 MHz in the shortest interval of time (74 min; Extended Data Fig. 1) to calculate the dispersion measure. We aligned these observations using a period of 1,091.1690 s, then ran dedispersion trials in steps of 0.5 over the range 50–60 pc cm^{-3}, finding that 57 ± 1 pc cm^{-3} produced the best fit. Light curves (Fig. 1) were then produced for each observation by applying dedispersion and averaging the dynamic spectra along the frequency axis.

Polarization

Polarization analysis was performed following the methods of the Polarised GLEAM Survey[33,34]. From all observations with detections, only observations within the 170–230-MHz range were selected for the polarization analysis to avoid depolarization caused by the (40-kHz) channel width. We performed RM synthesis[35] on the time-averaged Q/U spectrum of each observation with the RM-Tools software (https://github.com/CIRADA-Tools/RM-Tools) to obtain the corresponding RM, fractional polarization and polarization angle (see Extended Data Fig. 6 for these results in context with the surrounding region of sky). To investigate any variation of the polarization angle within the pulse phase, we also performed RM synthesis on the Q/U spectrum of each time step for two high-signal-to-noise-ratio observations. We found that the polarization angle was constant with respect to time within and between observations (for example, the middle two panels of Fig. 3).

Period and period derivative

We used phase-dispersion minimization based on the Lafler–Kinman statistic[36–39] to quantify the periodicity of the pulses, using the package P4J (https://github.com/phuijse/P4J). This choice is motivated by the variable shape and amplitude of the pulses and the presence of large, irregular gaps in data (which occasionally truncate part of an observed pulse). Using this method, we found a clear peak in the periodogram with a period of 1,091.170 s.

The period obtained from the periodogram analysis above assumes that the period is constant (that is, $\dot{P} = 0$). To place constraints on $\dot{P}$, we performed a grid search of P and $\dot{P}$ values, centred on 1,091.170 s and 0 s s^{-1}, respectively, to find which pairs of values are consistent with the observed arrival times of the pulses. We searched over the ranges $1{,}091.150\ \mathrm{s} \le P \le 1{,}091.185\ \mathrm{s}$ and $-4 \times 10^{-9} \le \dot{P} \le 4 \times 10^{-9}$, aligning the pulses in pulse phase for each value pair and taking the peak flux density of the averaged pulses (the 'mean profile' in pulsar parlance) as our metric for goodness of alignment. Because different pulses were observed in different frequency bands, each was normalized to a common frequency of 154 MHz using $\alpha = -1.16$ (see below), before averaging.

As shown in Extended Data Fig. 2, the resulting P and $\dot{P}$ were degenerate, as expected due to the 3-month time window of measurements and the evolving pulse profile. The maximum peak flux density 15.5 Jy corresponds to the values $P = 1{,}091.1690 \pm 0.0005$ s and $\dot{P} = 6 \times 10^{-10}$ s s^{-1}. The most important contour in Extended Data Fig. 2 is shown at 15 Jy to illustrate that there are multiple values of P and $\dot{P}$ that produce a similar flux density. Therefore, this analysis favours the range $0 < \dot{P} < 1.2 \times 10^{-9}$, that is, spin down is more likely than spin up. Note that the error on the source period is representative for any choice of $\dot{P}$ within this range, reflecting the width of the most notable contour in the period dimension.

Spectral index

Individual 30.72-MHz observations of GLEAM-X J162759.5-523504.3 lack the frequency coverage to determine an accurate spectral index, but since the flux density clearly varies with time, averaging over many observations is unlikely to yield a usable result. To obtain a good estimate, we used the same observations with which we calculated the dispersion measure: 1205008192 (72–103 MHz), 1205007112 (103–134 MHz), 1205011432 (139–170 MHz), 1205010352 (170–200 MHz) and 1205009272 (200–231 MHz); these are the observations taken on 13 March 2018 between 20:12 and 21:24 (Fig. 1), for which the pulse profile is reasonably consistent with time. After dedispersion and alignment on the source period, we obtained an average profile by averaging the data along the combined frequency axis (y axis in the right panel of Extended Data Fig. 1). From this, we selected the time steps in which the source was clearly on (time steps 0–100 in the right panel of Extended Data Fig. 1) and, for each frequency, determined the weighted average flux density, using the average profile as a weighting function.

Errors were calculated as the root-mean-squared noise of each slice for unflagged time steps during which the source was off, divided by the square root of the number of samples in the average flux-density measurement, added in quadrature with a 5% flux density calibration error. Extended Data Figure 3 shows the weighted averages and their errors plotted as a function of frequency. The drop-off at low frequencies is probably due to averaging over the strong ionospheric scintillation (the time-dependent striping visible at the top of Extended Data Fig. 1), and although the steepening at the higher frequencies may be intrinsic, the signal-to-noise ratio is low, so it is difficult to be sure.

Therefore, we used the measurements taken between 95 and 195 MHz and the scipy implementation of the Levenberg–Marquardt least-squares fit to determine a radio spectral index of $\alpha = -1.16 \pm 0.04$, where the flux density $S_\nu \propto \nu^\alpha$. The reduced χ^2 of the fit is 1.86.

Error on the distance estimate

Models of the Galactic electron density can be used to convert the dispersion measure into a distance. YMW16, the most recent model[4], derives a relative distance error $\frac{D_{\rm m}-D_{\rm i}}{D_{\rm i}}$ using 189 pulsars for which distances are known. $D_{\rm m}$ is the model distance based on the observed dispersion measure and $D_{\rm i}$ is the independently determined distance (for example, by parallax). For their sample, the root mean square of the relative distance error is 0.398. From version 1.65 of the Australia Telescope National Facility Pulsar Catalogue[40], we extracted data for the five pulsars with independently measured distances within 10° of GLEAM-X J162759.5-523504.3. For these pulsars, we found that the root mean square of the relative distance error is 0.393. Thus, we conclude that there is an approximately 40% error on the estimated distance of 1.3 kpc.

Position measurement

At radio frequencies, the apparent source position measured by an interferometer may be shifted by an angular offset $\Delta\theta$ by the ionosphere, proportional to the transverse gradient $\nabla_\perp$ of the total electron content towards the source and the square of the wavelength at which the observations were taken. To determine an accurate position for GLEAM-X J162759.5-523504.3, we used observation 1205009272, taken at the highest frequency band, 200–231 MHz, on a quiet night during which ionospheric distortions were minimized, and imaging just the 30-s subset of the observation during a high-signal-to-noise-ratio pulse. We used the software fits_warp[41] (https://github.com/nhurleywalker/fits_warp) to calculate the local position shift based on the apparent shifts of nearby, compact, bright calibrator sources. The error was calculated as the mean residual offset of these nearby sources after the shift had been modelled and removed, that is, 2″. The derived position is right ascension $16^{\rm h}\,27^{\rm m}\,59.5^{\rm s}$, declination −52°35′04.3″.

Swift XRT observations

We observed GLEAM-X J162759.5-523504.3 with the Neil Gehrels Swift Observatory[42] for 2 ks with the XRT[43] in photon-counting mode. The observations were taken from 25 February 2021 16:34:00 to 25 February 2021 21:27:00 (coordinated universal time) and the observation ID was 00014085001. We reduced and analysed the data using HEAsoft v6.28 (ref. [44]) and xrtpipeline v0.13.5. There is no detection of a point source in any bands nor is there any indication of extended structure. We estimate a $3-\sigma$ upper limit of 5.6×10^{-3} ct s^{-1} for the count rate in the 0.3–10-keV band for GLEAM-X J162759.5-523504.3. Assuming a thermal spectrum (blackbody, $kT = 0.1$ keV), the upper limit in count rate corresponds to an absorbed flux of 1.5×10^{-13} erg s^{-1} cm^{-2} in the 0.3–10-keV band. Assuming a non-thermal spectrum ($E^{-\alpha}$; $\alpha = 2$, typical for magnetars[15]), the upper limit in count rate corresponds to an absorbed flux of 1.9×10^{-13} erg s^{-1} cm^{-2} in the 0.3–10-keV band. Extended Data Figure 4 shows the corresponding luminosity limit calculated as a function of kT.

Radio-luminosity calculation

Working under the assumption that GLEAM-X J162759.5-523504.3 is a pulsar or magnetar in order to determine its energetics, we can transform the observed flux density into a radio luminosity. To precisely determine the radio luminosity of a rotating magnetic neutron star, its geometry with respect to the observer needs to be known; this is often derived by examining the change in pulse phase with respect to time. In the case of GLEAM-X J162759.5-523504.3, the pulse phase is flat, similar to the case of the radio magnetar Swift J1818.0−1607 (ref. [45]). In this case, we cannot derive the geometry of the emission cone and, instead, interpret the flat phase as our line of sight just grazing the edge of the emission cone (that is, the impact angle between the line of sight and the magnetic axis is similar to the emission cone opening angle). This is qualitatively consistent with the pulse duty cycle of 30–60 s of activity in 1,091 s, which is approximately 3–6%. For pulsars with this duty cycle, for typical opening angles of 6°, the radio luminosity at 1.4 GHz is $7.4 \times 10^{30} \frac{D}{\rm kpc}^{2} \frac{S_{1.4\,{\rm GHz}}}{\rm Jy}$ erg s^{-1} (ref. [46]). GLEAM-X J162759.5-523504.3 produces pulses of peak flux densities of up to $S_{154{\rm MHz}} = 45$ Jy. Scaling this to 1.4 GHz by $\alpha = -1.16$, we would expect $S_{1.4{\rm GHz}} = 3.5$ Jy and, therefore, $L_{1.4\,{\rm GHz}} = 4 \times 10^{31}$ erg s^{-1}.

Long-term duty cycle

In 8 years of operation, the MWA has accumulated around 160 h of observing time that have pointing directions within 15° of GLEAM-X J162759.5-523504.3 and might, in principle, be sensitive to it. However, as the data span many different projects, array configurations, frequencies and observing modes, and processing data takes about 100 times longer than observing, searching these data thoroughly is a daunting task. Furthermore, only when the data are taken in a contiguous ~20-min block may emission from this source be ruled out. We first examined the data before the January–March 2018 activity window using the period of the source and found no emission from GLEAM-X J162759.5-523504.3 in December 2017 or April 2018. We searched five blocks of 20-min contiguous observations in May 2017, October 2017, November 2017, April 2018 and May 2018, finding no detections. Before May 2017 and after June 2018, the telescope was reconfigured into compact 'Hex' mode, a redundant-baseline configuration with very poor imaging quality, yielding poor constraints from data taken in that mode. We searched for suitable observations in the archive as early as possible (March 2014 and June 2014) and also took new observations (February 2021), finding no detections. There remains in the archive about 15 h of data in suitable contiguous 20-min blocks that may be searched in a future paper.

At the time of writing, the MWA has been in operation for 8 years and this source was only found to be active for 2 months in that time, yielding an estimate of the duty cycle of $\frac{60\text{ days active}}{3,000\text{ days searched}} = 2\%$. Alternatively, we could assume that the source was active any time that we have not thoroughly searched the data and, with the cooperation of a conspiratorial Universe, the duty cycle can trend towards 100%. Or, this might be the only time in the (unknown) lifetime of the source that it has produced an emission, resulting in a duty cycle trending towards 0%. It is also worth noting that the source may not be entirely inactive during our non-detections, but its pulsations may be below our detection threshold; follow-up with a more sensitive radio telescope would be illuminating. For this work, we use the estimate of a 2% long-term duty cycle for pulses above the detection threshold of the MWA.

Pulse-profile evolution and alignment

At first examination, the three pulses recorded on 3 January 2018 appear to be misaligned with the other pulses. However, the pulses recorded on 13 March 2018 show an early 'secondary' pulse preceding the main pulse by approximately 15 s. Aligned by our determined P and $\dot{P}$, the pulses from 3 January 2018 fit within the wide pulse profiles found on 13 March 2018 (Extended Data Fig. 5). We, therefore, suggest that there is no misalignment and, instead, the apparent effect is caused by pulse-profile evolution.

Data availability

Data that support this paper are available at the following public repository: https://github.com/nhurleywalker/GLEAM-X_Periodic_Transient. Further data products can be supplied by the authors on reasonable request.

Code availability

Code that supports this paper is available at the following public repository: https://github.com/nhurleywalker/GLEAM-X_Periodic_Transient. Figure 3 was generated using https://github.com/nhurleywalker/Transient_Phase_Space. Further code can be supplied by the authors on reasonable request.

25. Tingay, S. J. et al. The Murchison Widefield Array: the square kilometre array precursor at low radio frequencies. *Publ. Astron. Soc. Aust.* **30**, e007 (2013).
26. Wayth, R. B. et al. The Phase II Murchison Widefield Array: design overview. *Publ. Astron. Soc. Aust.* **35**, e033 (2018).
27. Wayth, R. B. et al. GLEAM: the Galactic and Extragalactic All-Sky MWA survey. *Publ. Astron. Soc. Aust.* **32**, e025 (2015).
28. Offringa, A. R. et al. Parametrizing Epoch of Reionization foregrounds: a deep survey of low-frequency point-source spectra with the Murchison Widefield Array. *Mon. Not. R. Astron. Soc.* **458**, 1057–1070 (2016).
29. Hurley-Walker, N. et al. Galactic and Extragalactic All-sky Murchison Widefield Array (GLEAM) survey II: galactic plane 345° < l < 67°, 180° < l < 240°. *Publ. Astron. Soc. Aust.* **36**, e047 (2019).
30. Offringa, A. R. et al. WSCLEAN: an implementation of a fast, generic wide-field imager for radio astronomy. *Mon. Not. R. Astron. Soc.* **444**, 606–619 (2014).
31. Sutinjo, A. et al. Understanding instrumental Stokes leakage in Murchison Widefield Array polarimetry. *Radio Sci.* **50**, 52–65 (2015).
32. Lenc, E. et al. The challenges of low-frequency radio polarimetry: lessons from the Murchison Widefield Array. *Publ. Astron. Soc. Aust.* **34**, e040 (2017).
33. Riseley, C. J. et al. The Polarised GLEAM Survey (POGS) I: first results from a low-frequency radio linear polarisation survey of the southern sky. *Publ. Astron. Soc. Aust.* **35**, e043 (2018).
34. Riseley, C. J. et al. The Polarised GLEAM Survey (POGS) II: results from an all-sky rotation measure synthesis survey at long wavelengths. *Publ. Astron. Soc. Aust.* **37**, e029 (2020).
35. Brentjens, M. A. & De Bruyn, A. Faraday rotation measure synthesis. *Astron. Astrophys.* **441**, 1217–1228 (2005).
36. Lafler, J. & Kinman, T. D. An RR Lyrae star survey with Ihe Lick 20-INCH Astrograph II. The calculation of RR Lyrae periods by electronic computer. *Astrophys. J. Suppl.* **11**, 216 (1965).
37. Stellingwerf, R. F. Period determination using phase dispersion minimization. *Astrophys. J.* **224**, 953–960 (1978).
38. Schwarzenberg-Czerny, A. Fast and statistically optimal period search in uneven sampled observations. *Astrophys. J. Lett.* **460**, L107 (1996).
39. Clarke, D. String/Rope length methods using the Lafler-Kinman statistic. *Astron. Astrophys.* **386**, 763–774 (2002).
40. Manchester, R. N., Hobbs, G. B., Teoh, A. & Hobbs, M. The Australia Telescope National Facility Pulsar Catalogue. *Astron. J* **129**, 1993–2006 (2005).
41. Hurley-Walker, N. & Hancock, P. J. De-distorting ionospheric effects in the image plane. *Astron. Comput.* **25**, 94–102 (2018).
42. Gehrels, N. et al. The Swift gamma-ray burst mission. *Astrophys. J.* **611**, 1005–1020 (2004).
43. Burrows, D. N. et al. The Swift X-ray telescope. *Space Sci. Rev.* **120**, 165–195 (2005).
44. NASA High Energy Astrophysics Science Archive Research Center (HEASARC). HEAsoft: Unified Release of FTOOLS and XANADU (2014).
45. Champion, D. et al. High-cadence observations and variable spin behaviour of magnetar Swift J1818.0–1607 after its outburst. *Mon. Not. R. Astron. Soc.* **498**, 6044–6056 (2020).
46. Lorimer, D. R. & Kramer, M. *Handbook of Pulsar Astronomy* (Cambridge Univ. Press, 2012).
47. Zhang, B., Harding, A. K. & Muslimov, A. G. Radio pulsar death line revisited: is PSR J2144–3933 anomalous? *Astrophys. J. Lett.* **531**, L135–L138 (2000).

Acknowledgements N.H.-W. is the recipient of an Australian Research Council Future Fellowship (project number FT190100231) and G.E.A. is the recipient of an Australian Research Council Discovery Early Career Researcher Award (project number DE180100346) funded by the Australian Government. This scientific work makes use of the Murchison Radio-astronomy Observatory, operated by CSIRO. We acknowledge the Wajarri Yamatji people as the traditional owners of the observatory site. Support for the operation of the Murchison Widefield Array is provided by the Australian Government (NCRIS), under a contract to Curtin University administered by Astronomy Australia Limited. We acknowledge the Pawsey Supercomputing Centre, which is supported by the Western Australian Government and the Australian Government. The National Radio Astronomy Observatory is a facility of the National Science Foundation operated under cooperative agreement by Associated Universities, Inc. This project was supported by resources and expertise provided by CSIRO IMT Scientific Computing. This work used resources of China SKA Regional Centre prototype funded by the National Key R&D Programme of China (2018YFA0404603) and Chinese Academy of Sciences (114231KYSB20170003).

Author contributions N.H.-W. calibrated and processed the data for the observations described herein, determined the position and flux density of the source and prepared the manuscript, with contributions from all co-authors. X.Z. processed all polarization data, including performing polarization calibration and analysis. A.B. and S.J.M. performed the analysis to derive the period and period derivative. A.B. performed the X-ray observations and analysis. S.J.M. calculated and applied the dispersion measure and barycentric corrections. T.N.O. developed the original detection methodology, performed the original archive search and made the initial discovery. P.J.H. helped to develop the detection methodology and provided supercomputing support. G.E.A. contributed to astrophysical calculations and interpretation of the data. T.J.G., G.H.H., J.S.M. and X.Z. determined polarization calibration methods. T.J.G. performed early refinement of the period estimate.

Competing interests The authors declare no competing interests.

Additional information

Correspondence and requests for materials should be addressed to N. Hurley-Walker.

Peer review information *Nature* thanks the anonymous reviewers for their contribution to the peer review of this work. Peer reviewer reports are available.

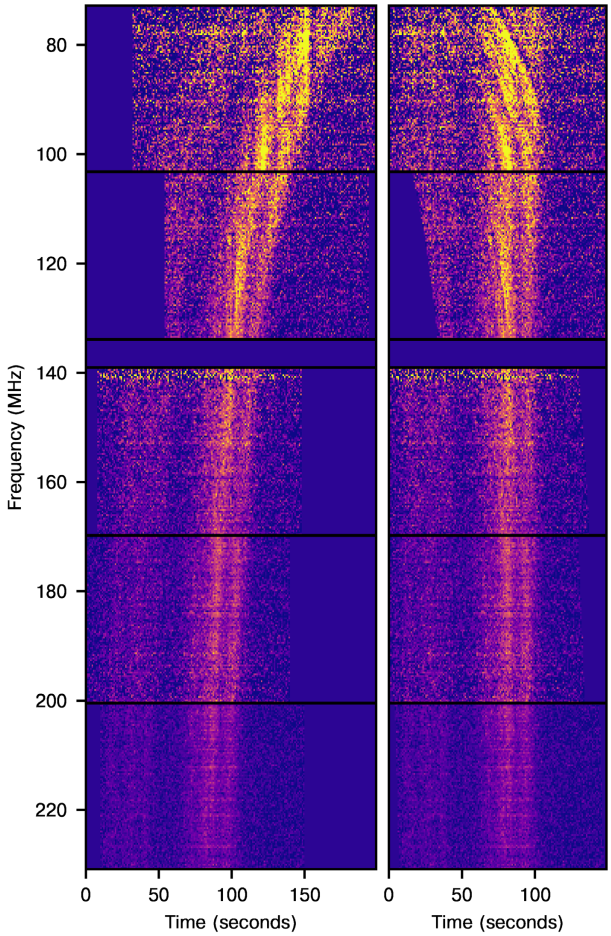

Extended Data Fig. 1 | Dynamic spectra of the observations used to calculate the dispersion measure. From top to bottom, separated by horizontal black lines, we show the observations 1205008192 (72–103 MHz), 1205007112 (103–134 MHz), 1205011432 (139–170 MHz), 1205010352 (170–200 MHz) and 1205009272 (200–231 MHz). These observations were taken on 13 March 2018 between 20:12 and 21:24 (see Fig. 1). The left panel shows the data aligned using a period of 1091.1690 s, whereas the right panel shows the same, including a dispersion correction of 57 pc cm^{-3}. Strong ionospheric scintillation is visible in the 72–103-MHz data, causing ripples in the brightness of the source over time.

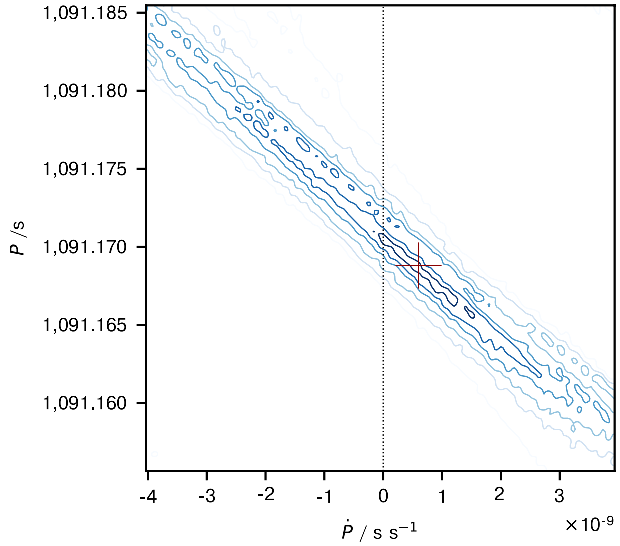

Extended Data Fig. 2 | The explored search space in *P* and $\dot{P}$ for the pulses recorded from GLEAM-X J162759.5-523504.3. The contours show the peak flux density of the mean profile at 154 MHz recovered at each combination of *P* (*y* axis) and $\dot{P}$ (*x* axis), in levels of 15, 14, 13, 12 and 11 Jy. The best-fit values of $P = 1{,}091.1690$ s and $\dot{P} = 6 \times 10^{-10}$ s s^{-1} are marked with a dark red '+'.

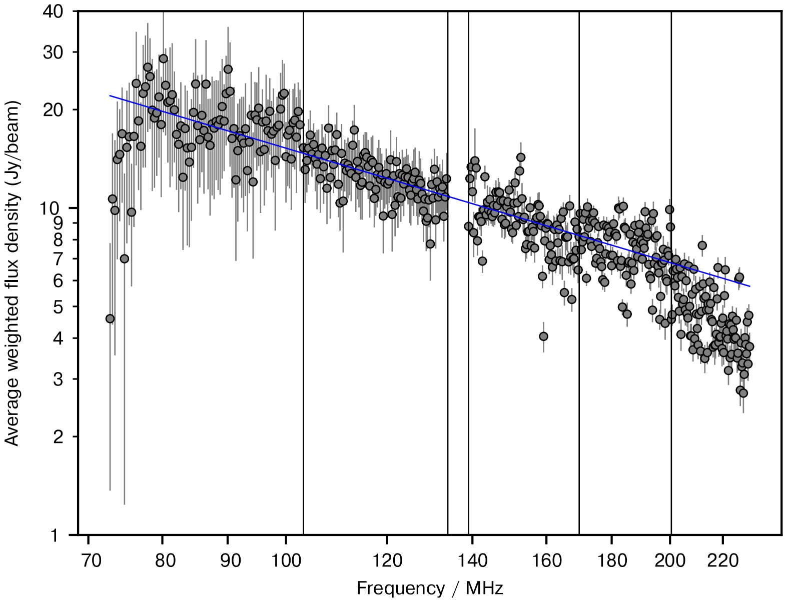

Extended Data Fig. 3 | The flux density of GLEAM-X J162759.5-523504.3 as a function of frequency. This is derived from the same observations shown in Extended Data Fig. 1. Points are determined via an average of the source profile in each frequency bin, weighting by the signal-to-noise ratio of the frequency-averaged profile. A power-law fit using the data spanning 95–195 MHz is shown in blue, with $\alpha = -1.16 \pm 0.04$.

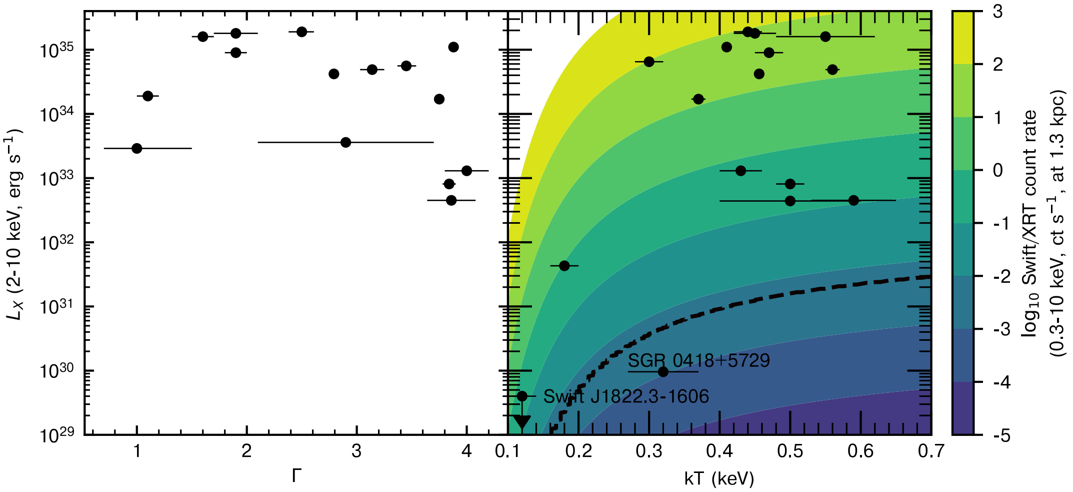

Extended Data Fig. 4 | X-ray luminosity and spectral properties of magnetars[15] compared with the X-ray luminosity limits of GLEAM-X J162759.5-523504.3. The two faintest known magnetars are labelled. The coloured contours represent expected Swift XRT count rates for putative X-ray luminosities and blackbody temperatures for a source at 1.3 kpc, assuming a hydrogen column density of $N_{\mathrm{H}} \approx 2 \times 10^{21}$ cm^{-2}. The grey dashed line represents the implied luminosity upper limit for GLEAM-X J162759.5-523504.3 based on the $3-\sigma$ upper limit obtained from the Swift XRT observation. From the magnetar fundamental plane, we predict GLEAM-X J162759.5-523504.3 to have a quiescent luminosity 4.5 orders of magnitude lower than our limit from the Swift XRT.

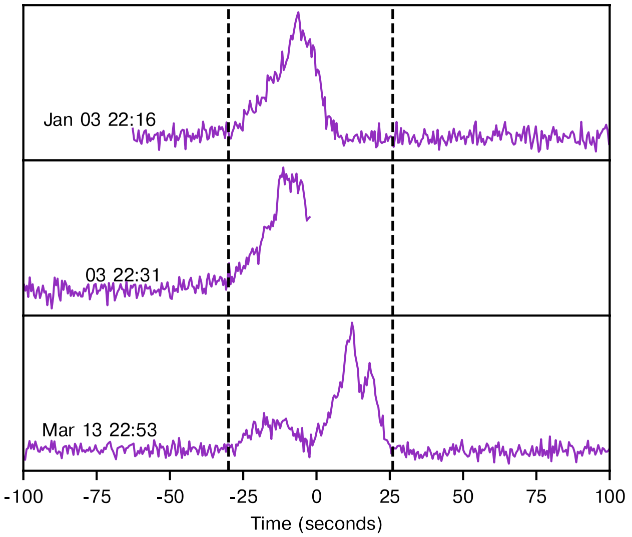

Extended Data Fig. 5 | Pulse profiles for the three detections on 3 January 2018 compared with a wide pulse detected on 14 March 2018. Barycentric corrections and dedispersion have been applied. The data are all taken at the same frequency, 170–200 MHz. Vertical dashed lines encapsulating the profile found on 13 March 2018 are overplotted to guide the eye.

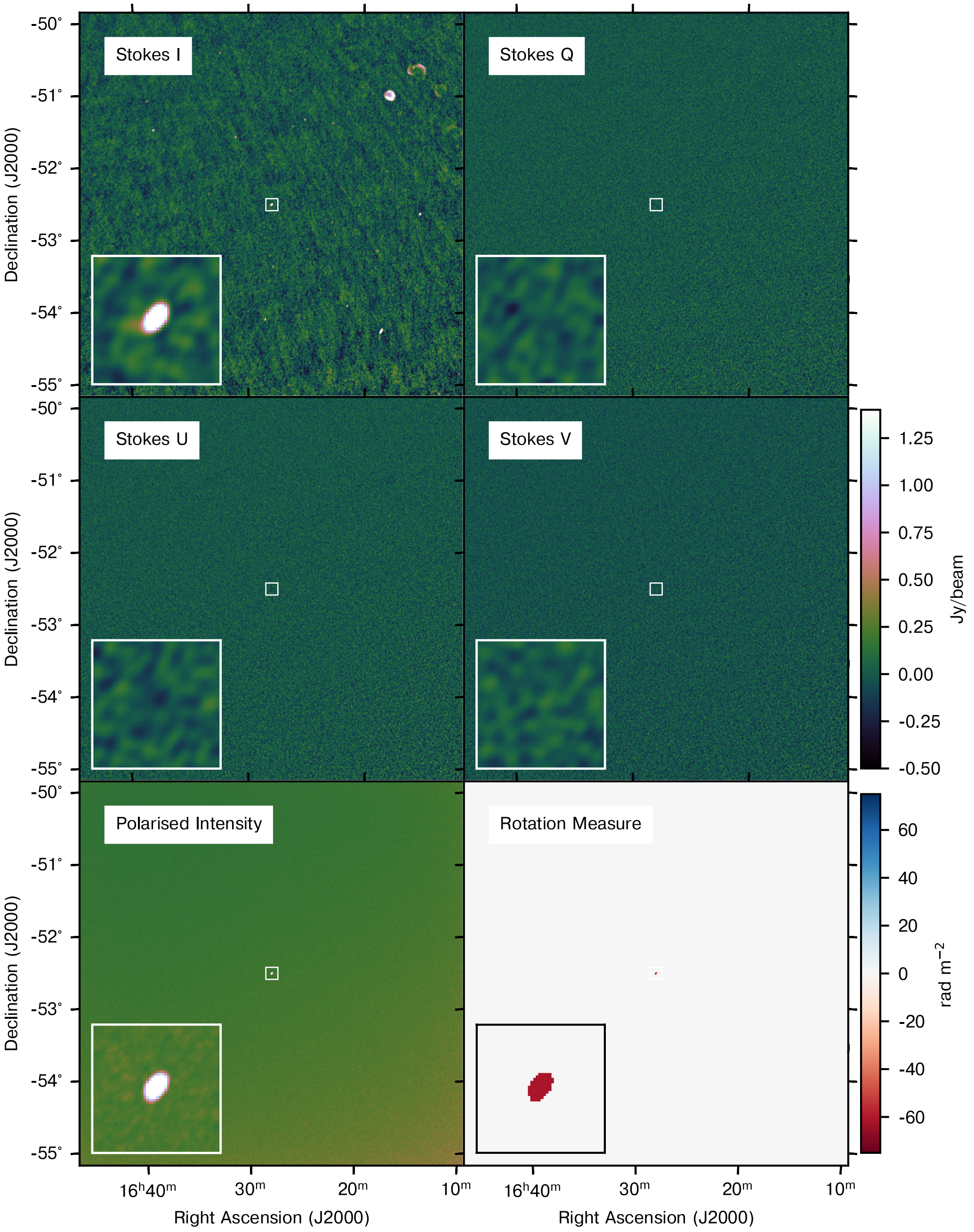

Extended Data Fig. 6 | Images in full Stokes and polarized intensity (in Jy beam^{-1}), and RM (in rad m^{-2}), of the region 5° × 5° around GLEAM-X J162759.5-523504.3. The images were made using observation 1200354592 on 18 January 2018 at 23:49, using only the interval where the source was producing emission. Faraday rotation over the imaged bandwidth of 30 MHz causes the Stokes Q, U and V emission to average to zero. The polarized intensity shows the maximum value of the RM spectrum. Where the polarized intensity is less than seven times the local noise, the corresponding RM value has been masked.

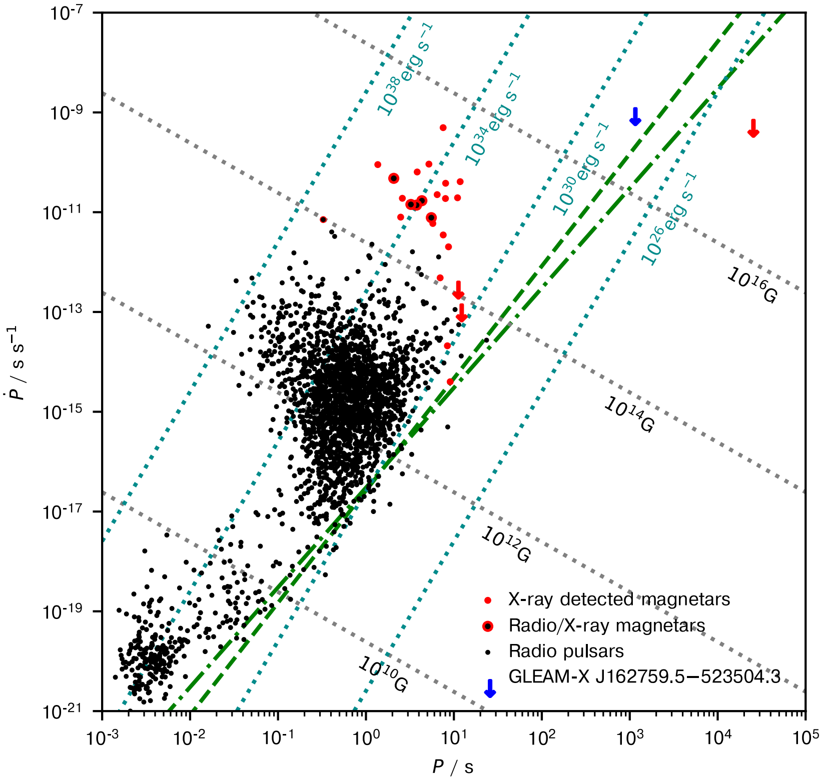

Extended Data Fig. 7 | A scatter plot of period derivative $\dot{P}$ against period P. GLEAM-X J162759.5-523504.3 is shown as a blue arrow with an upper limit on $\dot{P}$ (see Methods) in context with the known pulsars[40] (black dots), X-ray-detected magnetars[15] (red dots and arrows) and magnetars known to emit in both X-ray and radio frequencies (red circles around black dots). The slowest (and radio-quiet) X-ray magnetar 1E 161348−5055 is also shown with an upper limit on $\dot{P}$. The green dashed and dot-dashed lines correspond to the theoretical 'death lines' for pulsar radio emission for cases I and III calculated by Zhang et al.[47].